ARMY RESEARCH LABORATORY

The Sintering and Densification Behavior of an Iron Nanopowder Characterized by Comparative Methods

by Laszlo J. Kecskes, Robert H. Woodman, Samuel F. Trevino, Bradley R. Klotz, and S. Gary Hirsch

ARL-TR-2909 February 2003

NOTICES

Disclaimers

The findings in this report are not to be construed as an official Department of the Army position unless so designated by other authorized documents.

Citation of manufacturer's or trade names does not constitute an official endorsement or approval of the use thereof.

Destroy this report when it is no longer needed. Do not return it to the originator.

Army Research Laboratory
Aberdeen Proving Ground, MD 21005-5069

ARL-TR-2909 **February 2003**

The Sintering and Densification Behavior of an Iron Nanopowder Characterized by Comparative Methods

Laszlo J. Kecskes, Robert H. Woodman, Samuel F. Trevino, Bradley R. Klotz, and S. Gary Hirsch
Weapons and Materials Research Directorate, ARL

Acknowledgments

We note the assistance of Sara White at Nissei Sangyo America for the use of the field-emission scanning electron microscope, Dr. Bonnie Gersten with preliminary Brunauer, Emmett, and Teller (BMT), static and dynamic light scattering measurements, Kyu Cho for the x-ray diffraction measurement protocol development, and George Dewing for sample preparation and the operation of the plasma pressure compaction (P^2C). Bradley R. Klotz and Samuel G. Hirsch were supported in part by an appointment to the research participation program at the U.S. Army Research Laboratory (ARL) administered by the Oak Ridge Institute for Science and Education through an interagency agreement between the U.S. Department of Energy and ARL.

Contents

List of Figures

List of Tables

1. Introduction

1.1 Direct and Structural Applications of Nanosized Fe Precursor Powders

Fe powders have many applications that may be enhanced with the use of nanosized precursors. These include the catalysis of carbon nanotubes with superior electronic properties [1] and magnetorheological fluids [2]. Nanosized feed material is also expected to lower the consolidation temperature and improve the structural properties of iron bodies prepared by powder metallurgical techniques [3]. For instance, it has been shown recently that dense bodies of nanostructured iron (Fe) exhibit high-strain-rate mechanical behavior that is unlike that observed in coarser-grained material [4]. A popular, and arguably the most successful, method for preparation of nanograined material entails the comminution of micrometer-sized powder to nanoscale by high-energy ball milling [5]. The nanograined iron (Fe) cited by Jia et al. [4] was prepared by ball milling and sinter forging [6]. However, despite the promise of such evidence, the fabrication of large, fully dense, nanostructured bodies remains an unrealized goal.

A promising alternative to comminution is the direct synthesis of the nanopowder by microwave plasma synthesis (MPS). Fe bodies of 95% theoretical density (% TD) have been reported by moderate-pressure consolidation of precursor powder by plasma pressure compaction (P^2C) at 850 °C [3]. However, while the mean particle size of the powder was measured to be ~500 nm, the grain size of the final part was on the order of 10 μm. The primary advantage of P^2C is the ability to apply large direct currents (DCs) and alternating currents (ACs) through a powder sample, causing the formation of a plasma arc, whereby the interior temperatures rise rapidly. The plasma causes the evolution of impurities, and a simultaneous application of moderate pressure densifies the sample material. Detailed descriptions of P^2C, also known as plasma activated sintering (PAS), have been detailed by Groza [7] and Jones et al. [8].

1.2 Characterization of Nanosized Precursor Powders

In order to assess the contributions of nanopowders compared with larger-sized precursor powders, the particle morphology, size, and distribution must be known or evaluated. A number of books and articles address the topic of particle size measurement [9–11]. Only a few of these reports have dealt with the difficulties and limitations encountered in determining the particle size of nanopowders [12].

Many of the currently available particle size measurement techniques were designed for micrometer- and submicrometer-sized particles. While established off-the-shelf, canned methods offer ease of operation and minimal sample preparation, they still have limited applicability to nanopowders. For instance, field-emission scanning electron microscopy (FESEM) and other electron or optical microscopy techniques analyze small samples that may not be representative of the powder. In gas adsorption methods such as Brunauer, Emmett, and

Teller (BET) analysis, measurement can be done on a representative sample. However, adsorption of nitrogen or capillary condensation in interparticle voids can result in erroneous measurements [13].

Light scattering methods (e.g., dynamic light scattering [DLS] and static laser scattering [SLS]) have been developed for rapid measurement of particle size and size distributions of submicrometer-sized powders. Such methods measure either the spatial or the temporal variation of scattered light. In SLS, particles suspended in a fluid are exposed to a laser, and the amount of light scattered and the scattering angle are measured. Once calibrations of the response coefficients of the scattering light and detectors are known, the measured intensity distribution of the scattered light can be converted into a particle size distribution. It may be noted that it is difficult to collect light at high scatter angles associated with nanoparticles. As a result, the static method is limited to a practical size range of 20 nm–1000 μm.

In contrast, DLS is used for finer particles with a range of 3 nm–6 μm. In this method, the Brownian motion of the dispersed particles in the suspending fluid causes a Doppler shift of the incident beam. Consequently, the scattered light has a different temporal distribution than that of the incoming light. Iterative fitting operations of known frequency distribution functions (of particles with various known sizes) are applied to that of the unknown frequency distribution to obtain the unknown particle size.

Another challenge posed by nanosized powders is the preparation of dispersions. Such powders often do not wet or deagglomerate in the dispersing fluid medium. Pretreatment to deflocculate the nanopowder may require dispersants that need to be selected based on the surface chemistry of the powders. The powder suspension often requires a homogenization procedure (e.g., ultrasonics) to further break up aggregates. However, this process could also break up physically welded agglomerates, skewing the true particle size distribution of the sample.

Crystallography or diffraction-based techniques (e.g., x-ray diffraction [XRD] and neutron diffraction [ND]) determine crystallite size. If the nanopowder is polycrystalline, the result may be different than the apparent particle size [14]. Small angle neutron scattering (SANS) or small-angle x-ray scattering (SAXS) [12] can theoretically provide information about aggregate size, particle morphology, size distribution, surface area, total pore volume, and the thickness of a surface layer. However, the size range is limited from 1 nm to ~300 μm (1 nm to 2 μm for SAXS). This means that a prescreening for larger particles should be done. If the particles are very uniform in both size and shape, it is difficult to determine the size and shape of the powders from SANS alone.

1.3 Objectives

The primary objective of this effort was to use a wide range of analytical techniques such as FESEM, TEM, BET, DLS, SLS, XRD, and SANS/ND in conjunction with one another to characterize the particle size, particle morphology, and/or distributions of the MPS nanosized Fe

powder. Additionally, it was hoped that during the use of these methods, one would emerge as an effective screening tool for the evaluation of nanopowders. In other words, one that requires the least amount of preparation and analysis, but is most efficient in conveying an overall description of the sample.

To further examine the suitability of such nanopowder as raw material for the preparation of nanograined bodies, compacts of MPS Fe nanopowder were pressureless sintered in an H_2 atmosphere at various temperatures. The primary objective was to correlate the precursor powder characteristics and properties with sintering behavior and final microstructure. Additionally, evidence of enhanced low-temperature sintering, if any, was of interest. However, results showed that without the application of pressure, there was difficulty in attaining full density samples. Subsequently, several additional attempts were made to further densify the Fe using P^2C. Density of the sintered compacts was determined by mercury pycnometry, and the microstructure examined by scanning electron microscopy (SEM). The sintering results in context of the precursor characteristics, with implications for the production of bulk samples, are discussed.

2. Experimental Procedures

A representative sample of Fe nanopowder, derived from microwave plasma synthesis [3], was obtained from Materials Modification Inc. (MMI), Fairfax, VA. The microwave synthesis of the nanopowder entailed the controlled decomposition of $Fe(CO)_5$ (iron pentacarbonyl) at 700 °C. To prevent pyrophoric oxidation, freshly synthesized powder was quenched in liquid nitrogen (LN_2).

2.1 Particle-Size Characterization Procedures

2.1.1 Electron Microscopy Techniques

FESEM was performed on a Hitachi S4700 F-SEM (Nissei Sangyo America, Gaithersburg, MD). Several attempts to obtain optimum imaging conditions resulted in selection of an electron energy of 5 kV. Lower kilovolt settings did not have the required resolution; higher kilovolt settings tended to penetrate into the particles too deeply, resulting in the loss of surface detail. Both lower SE(L) and upper SE(U) secondary electron detectors were used with a working distance ranging from 11.6 to 3 mm. The sample was prepared by sprinkling Fe onto a colloidal carbon-covered aluminum stub. The loose, excess powder was blown off with an air gun.

The TEM used was a JEOL JEM-3010 (Japan Electron Optics Laboratory, Peabody, MA). Samples were prepared by placing a dash of powder in 2 mL of ethanol and sonicating it for ~2 min, then a carbon-coated, standard 200-mesh (65 μm) copper grid was dipped into the

suspension. The powder sample was examined in bright-field imaging mode at an accelerating voltage of 150 kV.

2.1.2 Brunauer, Emmett, and Teller (BET) Surface Area Measurement

Nitrogen gas adsorption analysis was performed on an ASAP-2010 Accelerated Surface Area and Porosimetry System (Micromeritics, Norcross, GA). Samples were outgassed overnight at 200 °C under vacuum. Two separate samples were subjected to six-point BET surface area analysis. Additionally, a full adsorption isotherm was collected from one of the samples.

The adsorption data offered no evidence of microporosity in the powder. Therefore, calculation of the equivalent area diameter yielded a meaningful value for particle size. Equation (1) depicts that S_{BET}, the surface area from the BET measurement, is inversely related to the particle radius:

$$r = 3\,[\rho(S_{BET})]^{-1}, \quad (1)$$

where r is the sphere radius and ρ is the density of Fe.

2.1.3 Light Scattering Methods

SLS was performed on an LA-910 (Horiba, Irvine, CA) using a flow cell. DLS was performed on a Horiba LB-500 (Horiba, Irvine, CA) in a stationary quartz cell. Preliminary attempts to disperse Fe in H_2O with a microfluidizer (Microfluidics, Newton, MA) or titanium microtip ultrasonic probe for 10–60 s were unsuccessful. In a more effective dispersion method, 0.1 weight-percent of sodium hexametaphosphate [$(Na(PO_3))_6$] was dissolved in deionized water. Approximately 0.023 g of nanosized Fe powder was dispersed in 20 mL of the base solution. The powder dispersion was sonicated for 10 min at 80 W, boiled for 5 min, and sonicated again for 10 min to break up the powder sample. Two SLS samples and one DLS sample were taken from this suspension.

2.1.4 X-ray Diffraction (XRD) Analysis

XRD analysis for determination of particle size was performed using Cu-Kα radiation on a fixed optics, APD-1700 Automated Powder Diffractometer System (Philips, Natick, MA). Generator settings were 45 kV and 40 mA. For the Fe powder, the four most intense peaks, [(110), 44.67°], [(200), 65.02°], [(211), 82.33°] and [(220), 98.94°], were scanned. Preliminary scans were made to determine the dwell time, step size, and scan range such that the net peak height under each peak was at least 10,000 counts. All peaks were scanned with a step size of 0.010° and 2Θ range of at least ±3°. The instrumental broadening was determined by using two commercially available powders: −100-Mesh Fe (Alfa-Aesar, Ward Hill, MA) and an LaB_6 XRD-broadening standard (National Institute of Standards and Technology, Gaithersburg, MD). The −100-Mesh Fe powder was annealed at 450 °C for 2 hr in H_2 to remove any residual stress. Specifically, characteristic peaks of LaB_6 near the four nanosized Fe peaks were scanned: [(200), 43.52°], [(220), 63.22°], [(320), 83.85°], and [(410), 99.64°]. Because of the narrowness of the LaB_6 peaks, a finer step size of 0.005° was used. For the −100-Mesh Fe powder, the same

aforementioned peaks as those for the nanosized Fe powder were scanned. It was assumed that the measured peak broadening of the LaB_6 peaks was attributable to instrumental broadening only. Despite the annealing treatment, the -100-Mesh Fe showed a greater broadening than LaB_6. Consequently, its use was discontinued. After subtracting the instrumental broadening contribution from the nanosized Fe peaks, Warren's or Scherrer's equation [14, 15] was used to determine the particle size.

2.1.5 Neutron-Based Methods

Both SANS and neutron diffraction (ND) were performed at the Center for Neutron Research (CNR) at the National Institute of Standards and Technology (NIST) (Gaithersburg, MD) on the 30-m SANS and BT1 powder diffractometer instruments, respectively.

Briefly, ND was performed on a multidetector instrument where the neutrons are scattered by single crystal monochromators [Cu (311) and Si (531) with wavelengths, λ_{ND}, of 0.15405 and 0.15904 nm, respectively] at a fixed scattering angle. The neutron detector was composed of an array of 32 detectors separated by 5° in scattering angle. The widths of the collimators before and after the monochromator, and before the detectors are 7, 20, and 7 min of arc, respectively. The measurement was taken with 0.05° steps in 2Θ. Measurements of particle size, local strain, and lattice strain distributions were obtained from the intensity, I_{ND}, vs. Q_{ND} [$4\pi\sin(\Theta)/\lambda$] data. A more detailed description of the instrument, data collection, and analysis is provided in the Appendix.

For SANS, a mechanical velocity selector rendered the "cold neutrons" from the source monochromatic and a monochromator provided wavelength resolution from 10% to 20% and wavelengths, λ_{SANS}, of 0.5–1.2 nm. The incident direction was defined by two circular pinholes. The scattered neutron direction was defined by a 5-mm spatial resolution, two-dimensional (2-D) detector located perpendicular to the incident direction. The angular range available (and therefore the reciprocal wave vector range, Q) was determined by the position of the detector with respect to the sample. The detector, placed at 1–15 m from the sample, could be laterally displaced by 25 cm. The distance between the incident pinholes was adjusted to match the resolution determined by the sample detector configuration. The sample was kept under vacuum so that the scattering length density of spheres was taken to be that of Fe (8.02×10^{-4} m^{-2}). The data were first analyzed using a uniform density sphere model. The data were then reanalyzed by a model of bimodal particle size distribution, as guided by the diffraction results. Each mode was represented by a Schulz distribution [14] whose parameters were a scale factor, I_{SANS}, a mean particle size, r, and a polydispersitivity, P. In the fitting process only I_{SANS} and P were allowed to vary. The value of the r used was obtained from the ND results.

2.2 Pressureless Sintering Experiments

The bulk tap density was determined by first weighing the as-received Fe powder, then dividing the weight by the filled container volume.

Green compacts were made from the Fe nanopowder at a range of compaction pressures under ambient laboratory conditions in a uniaxial die. Only about 1 g of powder was used for each compact. During handling, the Fe nanopowder was very fluid, readily flowed, forming a dust cloud. Extreme care had to be used to prevent the pyrophoric oxidation of the powder. In many instances the powder rapidly oxidized into red, ferric oxide, Fe_2O_3. The density of the green compact was measured by dividing its mass by the calculated volume, based on measurements of the compact thickness and diameter. After a trial and error determination of the optimum pressure to achieve the highest compact density without an oxidation reaction, several compacts were pressed at 55 MPa (8000 psi) for the pressureless sintering studies.

Pressureless sintering was performed at 300°, 500°, 700°, or 900 °C for 30 min under a 10 L/min flow of dry H_2. The sintered pellets were halved; one half was used to determine pellet density. The other half was mounted and polished for SEM examination; the polished surfaces were etched with 2% Nital to reveal the microstructure. Initial density measurements of the sintered samples, using Archimedes' principle, were discontinued after the discovery of very large errors, introduced by the smallness of the specimen volumes. The sample densities were then remeasured using mercury pycnometry in an Autopore IV Model-9510 Mercury Porosimeter Analyzer (Micromeritics, Norcross, GA).

2.3 P^2C Experiments

Similarly sized green compacts were loaded in a 1.27-cm inner diameter graphite die assembly. A two-color optical pyrometer was focused on the center of the die to measure the external temperature as the power level through was raised. It is likely that the interior temperatures were higher. In each P^2C run, DC current was ramped at 100 A/min, such that the target temperature was reached in a few minutes. At the same time, a constant pressure of 127 MPa was applied to the samples. More detailed descriptions of the apparatus and its operation can be found in Klotz [16]. Higher pressures caused the dies to crack or shatter. When a predetermined time elapsed at the selected temperature, the current was ramped down to zero A and the pressure released. After cooling, the P^2C samples were extracted and analyzed in the same manner as those obtained from pressureless sintering.

3. Results

This research program was divided into three parts: characterization, pressureless sintering, and plasma pressure compaction. Each component of the work will be described separately.

3.1 Powder Characterization

Results of the characterization effort are summarized in Table 1. In turn, each method and the corresponding data are now described in detail.

Table 1. Summary of methods and results.

Method	Particle Size (nm)	Comments
FESEM/TEM	50–80; 300–1000	Bimodal
XRD	20	—
SANS/ND	24 and 64	Bimodal, Gaussian
BET	60	Type II Isotherm
SLS	500–8000	Bimodal
DLS	70	Gaussian

3.1.1 Electron Microscopy Techniques

Figures 1a and 1b depict FESEM images taken at 5 kV. The particle size appears to be 50–80 nm. It was difficult to locate any isolated Fe particles. Instead, the Fe grains appear to be fused to each other into chain-like tentacles that form dendritic agglomerates with sizes of 0.3–1 μm. It is also worthwhile to note that the high contact angles seen in the particle-particle necks reflect late-stage particle-particle sintering. Despite the high transparency of the particle chains (Figure 1c), TEM examination of the powder was nevertheless able to discern a finer substructure within the apparently coarser 50–80 nm grains. The approximate size, or lower limit, of the subgrains was at least 20 nm.

3.1.2 Brunauer, Emmett, and Teller (BET) Surface Area Measurement

Figure 2 shows the BET plots for the two samples. Both are linear with least-squares correlation coefficients >0.999. The linear BET plot corresponds to a BDTT Type II or Type IV isotherm. Microporous samples frequently exhibit a BDTT Type I isotherm also known as the Langmuir type [17]. Type I isotherms do not produce a linear fit in a BET plot. Furthermore, the value for the BET c constant was ~42 for each sample. If the powders were microporous, the value of this parameter would be higher (~200 or greater), reflecting the higher apparent adsorption energy in a microporous solid [17]. The linear BET plots and the values of the c constant both indicate that the powders are free of fine pores and that the effective diameter calculated from S_{BET} is indicative of particle size.

Results of the BET surface area analysis were 13870 and 15080 m^2/kg. Using a hard-sphere model and a 7870 kg/m^3 density for Fe, the equivalent radius was found to be 28 and 25 nm, respectively, which corresponds to a diameter range of 50–60 nm. This particle size appears consistent with the FESEM results.

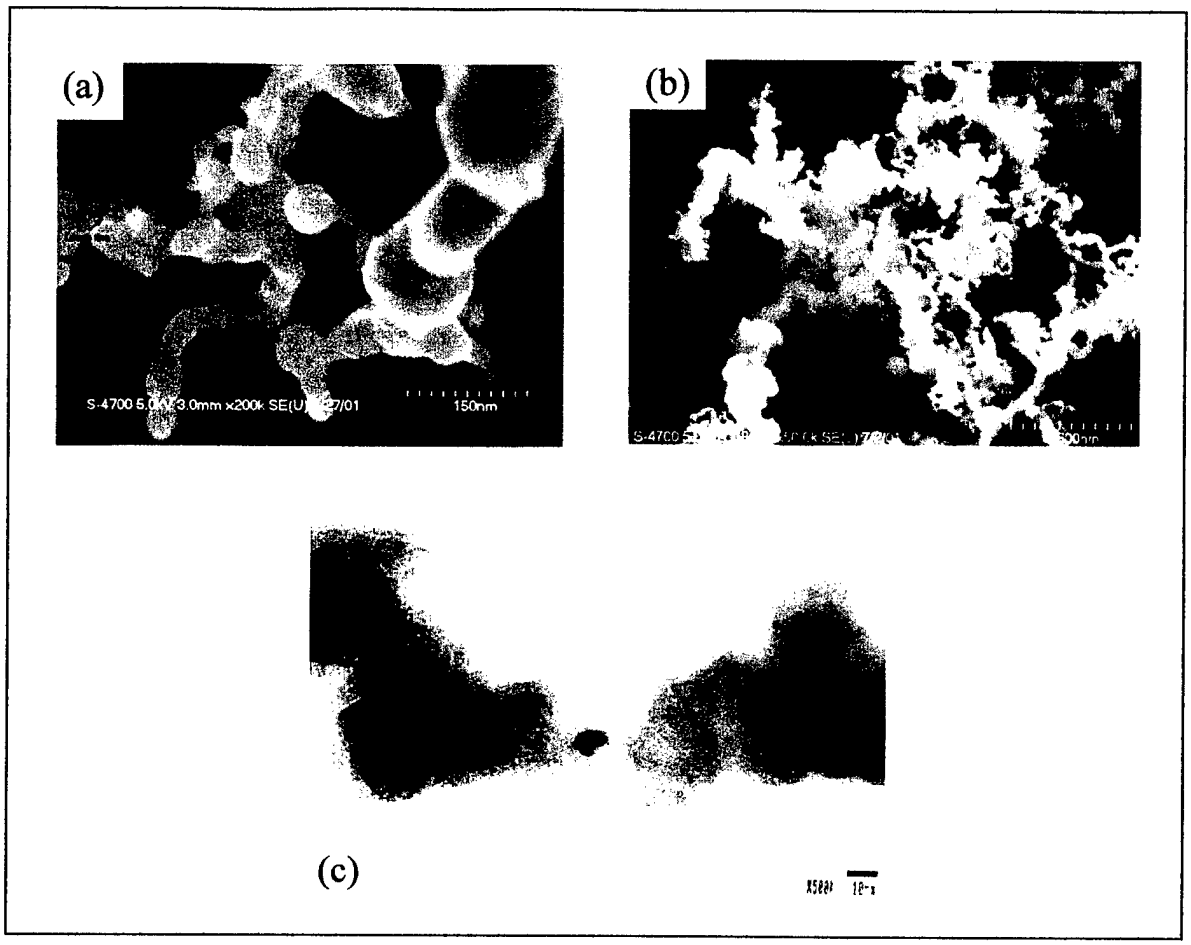

Figure 1. Electron microscopy of the Fe nanopowder. FESEM images show in (a) the individual nanometer-sized particles, and in (b) the dendritic agglomerates. Bright field TEM image of the particle substructure is shown in (c).

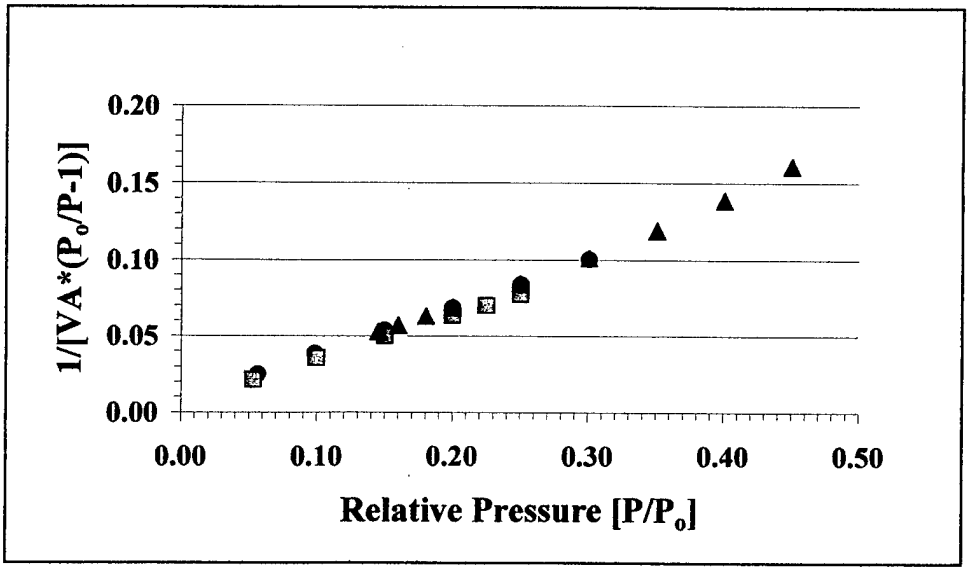

Figure 2. Type II BET surface area isotherm of the nanosized Fe.

3.1.3 Light Scattering Methods

Frequency distributions of particle size for SLS and DLS are shown in Figures 3a and 3b. From the various SLS measurements (Figure 3a), Fe particles appear bimodal with particles sizes that are much larger than the size determined from the previous methods. Results of five consecutive DLS measurements spread over a 20-min time span indicated a single particle size distribution of a mean particle size of 70 ± 7 nm.

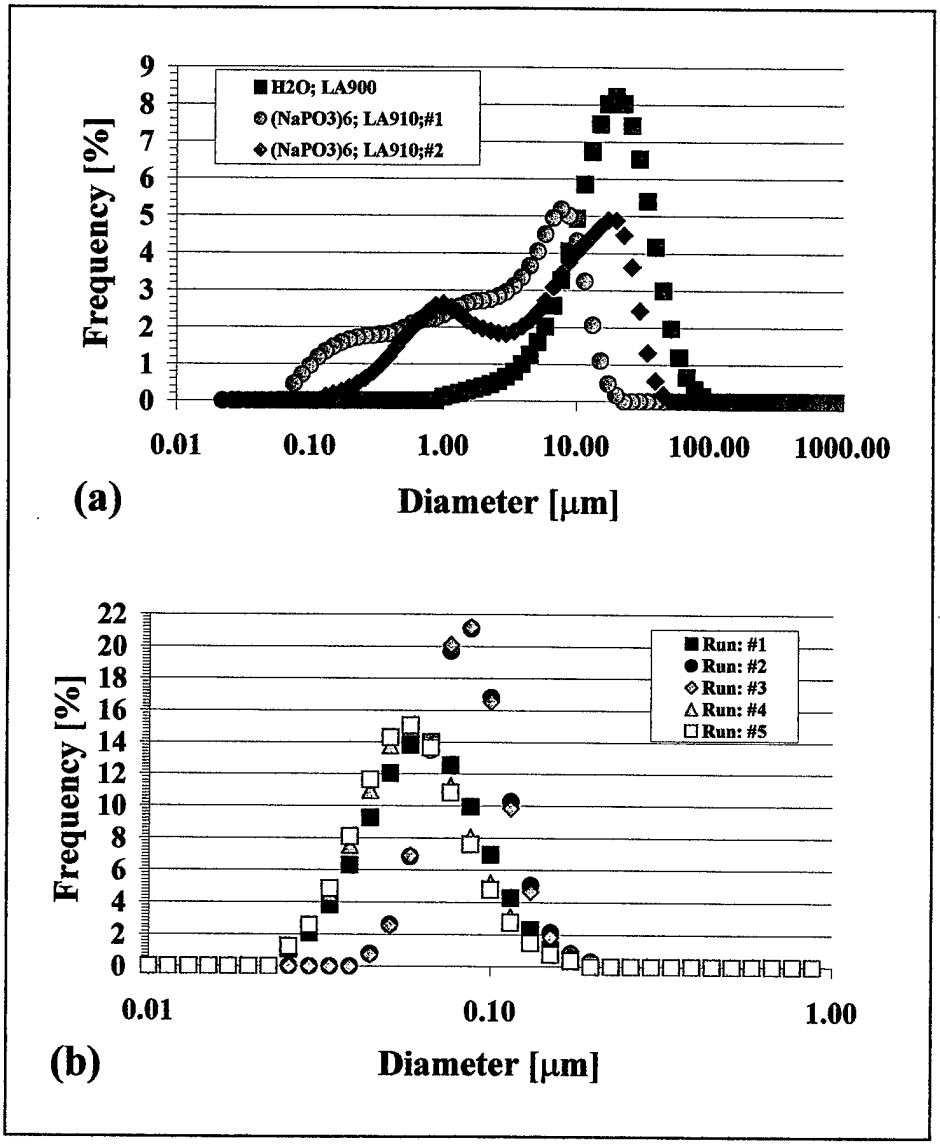

Figure 3. Laser scattering results: (a) frequency distribution from SLS and (b) frequency distribution from DLS.

3.1.4 X-ray Diffraction (XRD) Analysis

Typical XRD line-broadening profiles are shown with the LaB_6 (200) peak in Figure 4a, the −100-Mesh, annealed Fe (110) peak in Figure 4b, and the corresponding nanosized Fe (110) Fe

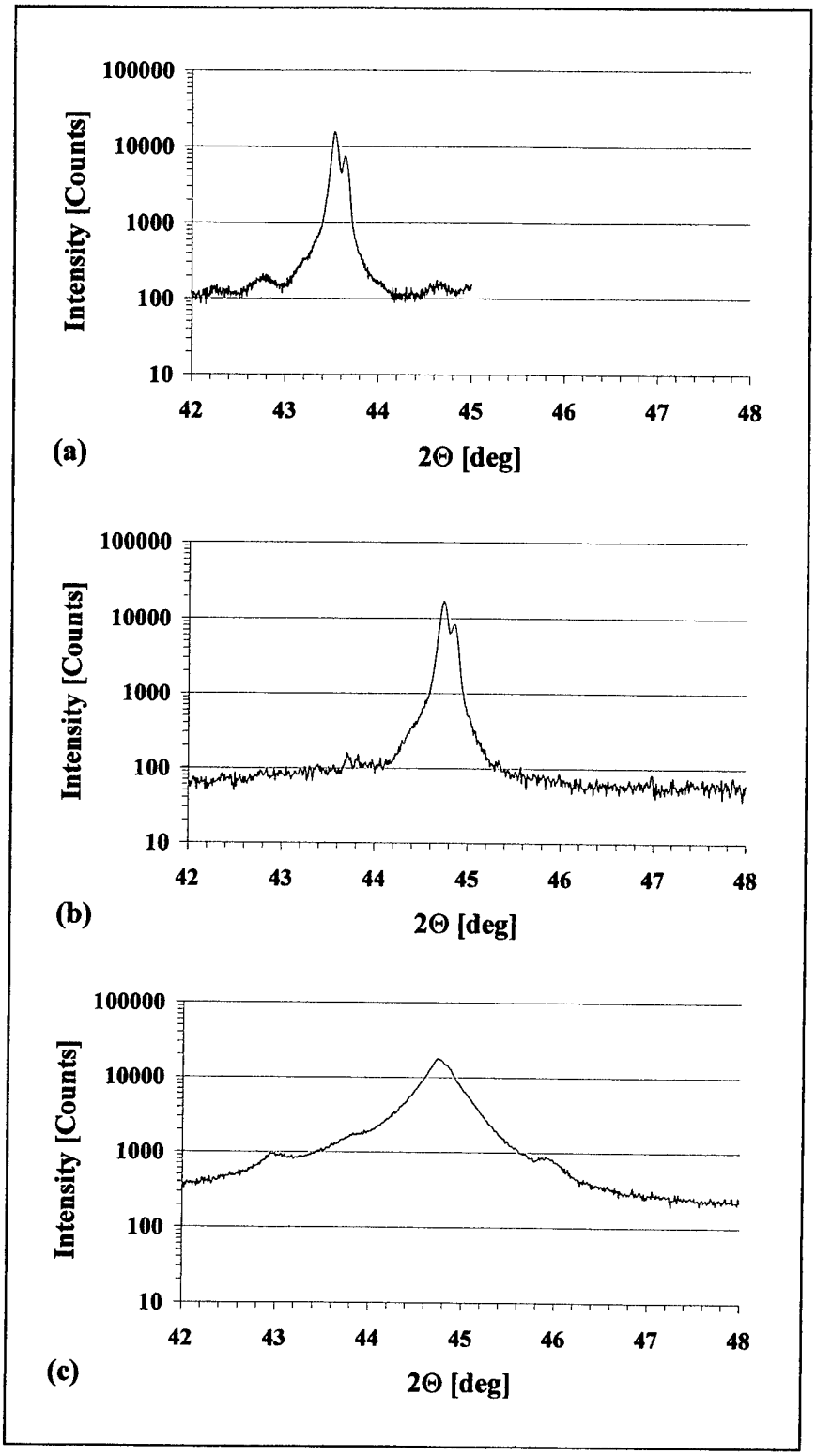

Figure 4. XRD scan line profiles: (a) (200) peak profile for the LaB_6 calibration standard, (b) (110) peak profile for the annealed -100-Mesh Fe powder, and (c) (110) peak profile for the Fe nanopowder.

peak in Figure 4c. The as-measured full width at half maximum (FWHM) for the three powders are graphed in Figure 5. Note that the -100-Mesh, annealed Fe and LaB_6 gave slightly larger-sized minimum peak widths. The remainder of the analysis, summarized in Table 2, entailed subtracting the instrumental FWHM from each of the four nanosized-Fe peaks. Using the Scherrer equation [15] yielded an average crystallite size of ~20 ± 3 nm. In contrast, Warren's method [14] yielded a slightly smaller size. Aside from the TEM results, these values were considerably less than those obtained by any of the other methods.

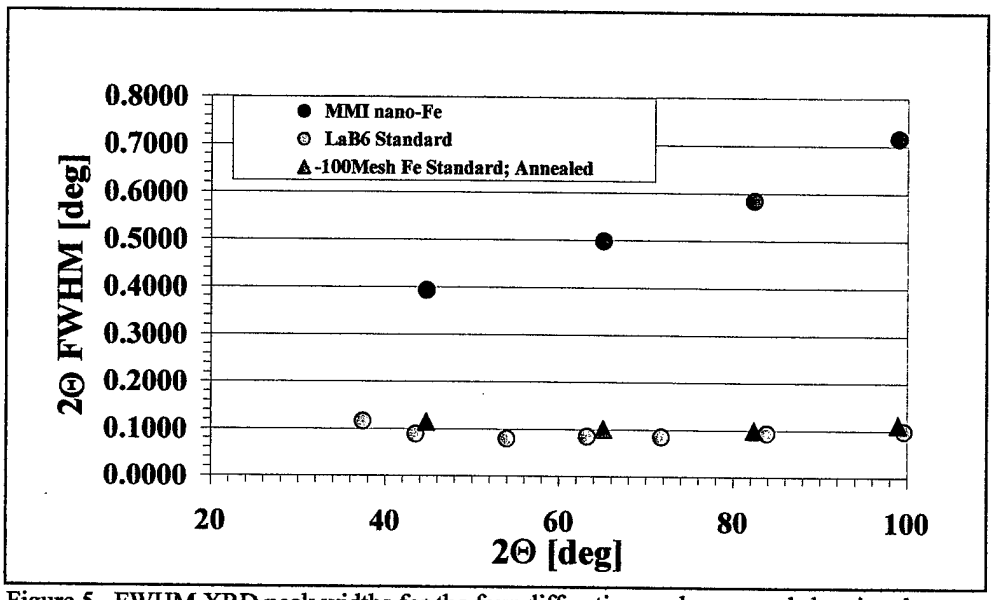

Figure 5. FWHM XRD peak widths for the four diffraction peaks scanned showing the results for all three powders.

Table 2. XRD analysis summary and results.

Peak	2Θ (deg)	2Θ (rad)	F (deg)	F (rad)	F –F(LaB_6) (rad)	$\sqrt{[F^2 - F(LaB_6)^2]}$ (rad)	Scherrer Size (nm)	Warren Size (nm)
LaB_6								
(200)	43.53	0.760	0.089	0.002	NA	NA	NA	NA
(220)	63.24	1.104	0.085	0.001	NA	NA	NA	NA
(320)	83.86	1.464	0.094	0.002	NA	NA	NA	NA
(410)	99.65	1.739	0.099	0.002	NA	NA	NA	NA
Nanosized Fe								
(110)	44.75	0.781	0.393	0.007	0.005	0.007	28	22
(200)	65.09	1.136	0.499	0.009	0.007	0.009	23	19
(211)	82.38	1.438	0.585	0.010	0.009	0.010	21	18
(220)	98.98	1.728	0.716	0.012	0.011	0.012	20	17

Note: NA = not applicable.

3.1.5 Neutron-Based Methods

In the measured ND pattern obtained from the Fe sample with the Cu (311) monochromator, each peak consists of two components: a narrow and broad peak at the same positions as shown in Figure 6 for the (110) Fe reflection. From ND, the narrow peak particle diameters were found to be 63 nm with a root mean square (RMS) strain of 0.028; the broad peak particle diameter was found to be 24 nm with an RMS strain of 0.165. The larger particles constituted 37% of the sample and comparatively did not have residual strain.

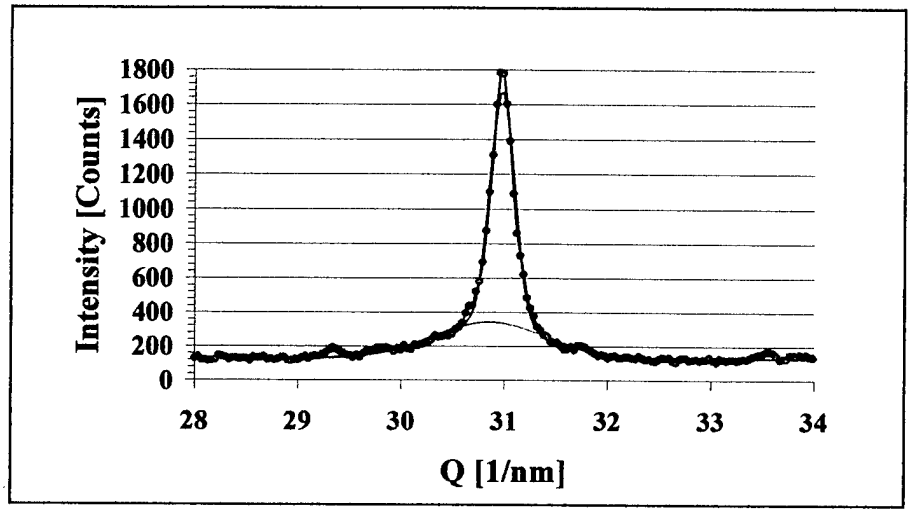

Figure 6. ND of the (110) Fe reflection. Note the presence of the two Gaussian fits under the peak

Figure 7a shows the SANS results of the fit to a bimodal distribution model. In the figure, the data are shown as open circles and the fits as solid lines. The two distributions are found by the information represented by the broad concave curvature at Q~0.001 nm and a convex curvature at Q~0.006 nm. The particle size distributions, P, for each of these components are shown in Figure 7b. The total distribution is included as well. The scale factors indicate that the large component is 47% of the total rather than the ratio resulting from the ND. However, this is not considered important enough to assert that the two data sets (ND and SANS) are not consistent.

It is clear from the results previously mentioned that the sample consists of at least a bimodal distribution of particle sizes that are not very narrow. The range of Q that was obtained here does not exclude the existence of even larger particles. The capabilities of each of the measurements are also clearly demonstrated. The diffraction can detect mean particle size and the effects of strain, whereas the SANS is sensitive to the particle size distribution. Each on its own is very useful but in combination provides a quite complete description of the sample. A detailed description of how the ND and SANS data were obtained is given in the Appendix.

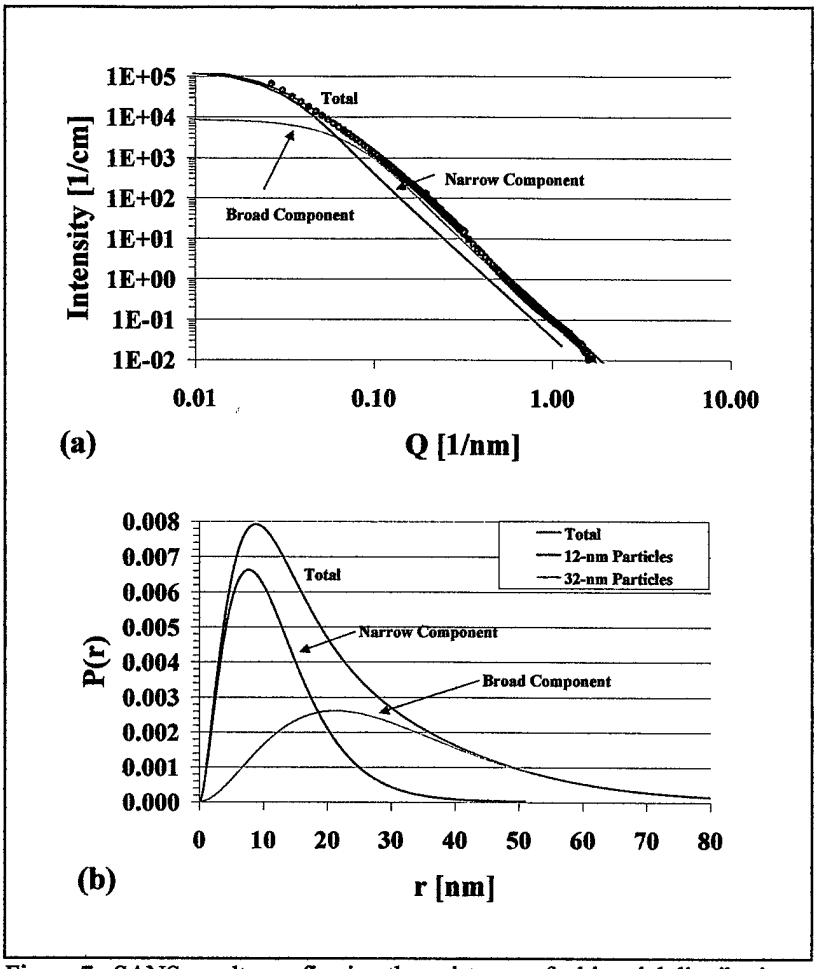

Figure 7. SANS results confirming the existence of a bimodal distribution of crystallites in the nano Fe: (a) overall scattering data and (b) relative distributions of the particle sizes.

3.2 Pressureless Sintering Results

Pressureless densification results are displayed in Figure 8 and summarized in Table 3. Apparently, full densification by pressureless sintering could not be achieved. Relatively high sample densities of ~90% TD were determined by the Archimedes method. However, upon remeasurement with mercury pycnometry, it was found that the densities were erroneous. The source of error was traced to a rather large error in the measurement of the sample volume; the correct densities (obtained with mercury pycnometry) are listed in Table 4.

The bulk density of the powder was 0.13 gcm^{-3}, or 1.6% TD of Fe. Green density of the compacts was ~40% TD. Furthermore, the powder did not compact normally, but proved to be "springy." That is, the compacted powder exhibited sufficient springback to be ejected from the die during filling. Furthermore, the powder proved to be pyrophoric, sometimes combusting during die filling or compaction.

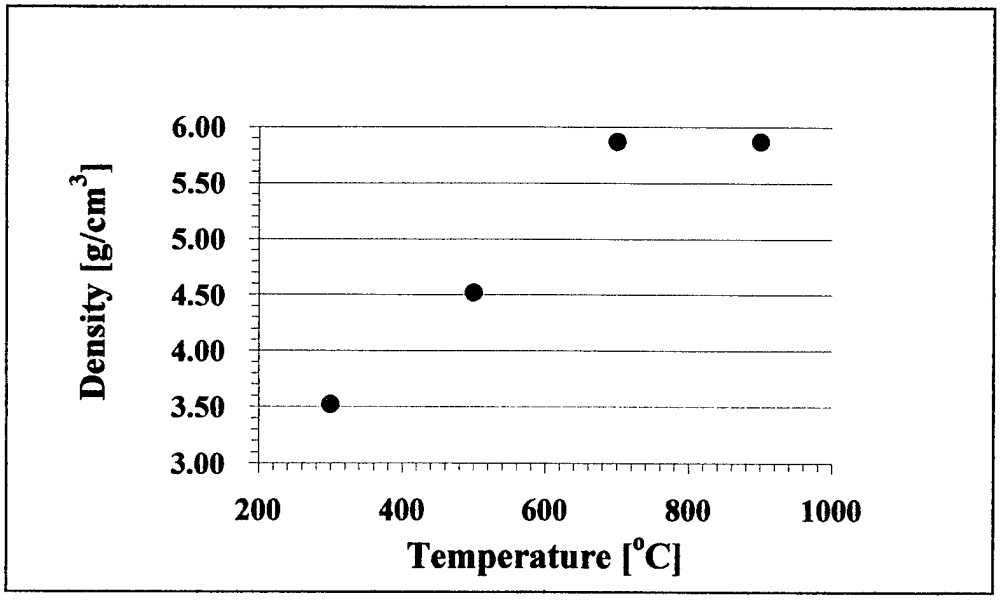

Figure 8. Pressureless sintered (pycnometer) density vs. temperature for the nanosized Fe powder.

Table 3. Pressureless sintering results.

Temperature (°C)	Archimedes Density (gcm^{-3})	Density (% TD)
300	7.25	92.1
500	7.00	88.9
700	6.50	82.6
900	7.15	90.9

Table 4. Corrected pressureless sintering results.

Temperature (°C)	Pycnometry Density (gcm^{-3})	Density (% TD)	Grain Size (μm)
300	3.52	44.7	0.05
500	4.52	57.4	1
700	5.87	74.6	5
900	5.87	74.6	50

Regardless of the sintering temperature, all four of the consolidated pellets delaminated, though, the appearance of the compacts improved with increasing temperatures. At the lower two temperatures, the pellets were heavily delaminated, black, and rough. The extent of delamination seemed to decrease with increasing temperature. At the higher two temperatures (700° and 900 °C), the pellets had only one or two lateral delaminations, but were blistered, with a silvery exterior surface. Interior surfaces were also shiny.

Shown in Figure 9, low- and high-magnification SEMs of the polished and etched surfaces of the pellet cross sections, depict the evolution of the sintered microstructure. At 300 °C, there is very little or no coarsening of the individual Fe nanoparticle grains (Figures 9a and 9b). Note that the dendritic aggregate structure of the Fe clusters is still mostly present. However, in some isolated areas, there is extreme coarsening. Figure 10 shows an enlarged view of the onset of sintering with bridging and necking between adjacent particles as the dendrite arms collapse. As shown in Figures 9c and 9d, at 500 °C, a banded structure appears, with alternating low- and high-density regions that most likely are associated with the macroscopic delamination of the sample. At this temperature, the onset of the dendritic nanoparticle coarsening is also evident. In contrast, as depicted in Figures 9e and 9f, once the temperature exceeds 700 °C, any remaining evidence of the initial dendritic structure and morphology is lost. Instead, gross rearrangement, with extensive secondary recrystallization and growth, occurs. Nevertheless, submicrometer voids or closed pores remain at the triple points between the recrystallized grains. Impurities, such as oxides, would be expected to segregate at the grain boundaries, and thus cause high contrast. The absence of such contrast at the grain boundaries indicates this powder is relatively free of contamination. Finally, in Figures 9g and 9h, heterogeneous grain growth at 900 °C of the recrystallized Fe grains dominates the pellet's microstructure. (There are a few polishing scratches in some of the softer grains.) Submicrometer voids also coalesce into 10-μm void agglomerates or void bands.

Despite a lack of densification, as was shown in the Table 4, the grain size of the consolidated Fe pellets dramatically increases with temperature. Shown in Figure 11, a semi-logarithmic graph of the average grain size vs. inverse sintering temperature appears fairly linear. Assuming an Arrhenius behavior for atom diffusion and associated grain growth, a least squares fit to the data yields an activation energy of 62 ± 6 kJ/mol. This is only one-fourth of that for the self-diffusion of Fe [18].

3.3 P^2C Results

Unlike the pressureless sintered samples, the P^2C samples were not delaminated. Results of the experiments are listed in Table 5. As apparent, the variations of time or temperature have a relatively minor effect on the overall density of the samples. Under moderate pressure, the initially isotropic agglomerates form highly oriented (transverse to the compaction axis), filamentary structures of alternating dense and porous strata (Figure 12). Low- and high-magnification images at 600 °C (Figures 12a and 12b) show that the interior of these filaments consists of dendritic aggregates that sintered into a coarsened, yet porous spongy structure. Note the formation of anomalously more dense regions. A comparison of the two samples at 600 °C, shows that at low temperatures the effect of time is negligible on the microstructure (Figures 12c and 12d). At higher temperatures, similar image pairs, especially at 800° and 1000 °C (Figures 12e–12h), show that these filamentary layers grow denser. The interior of these bands

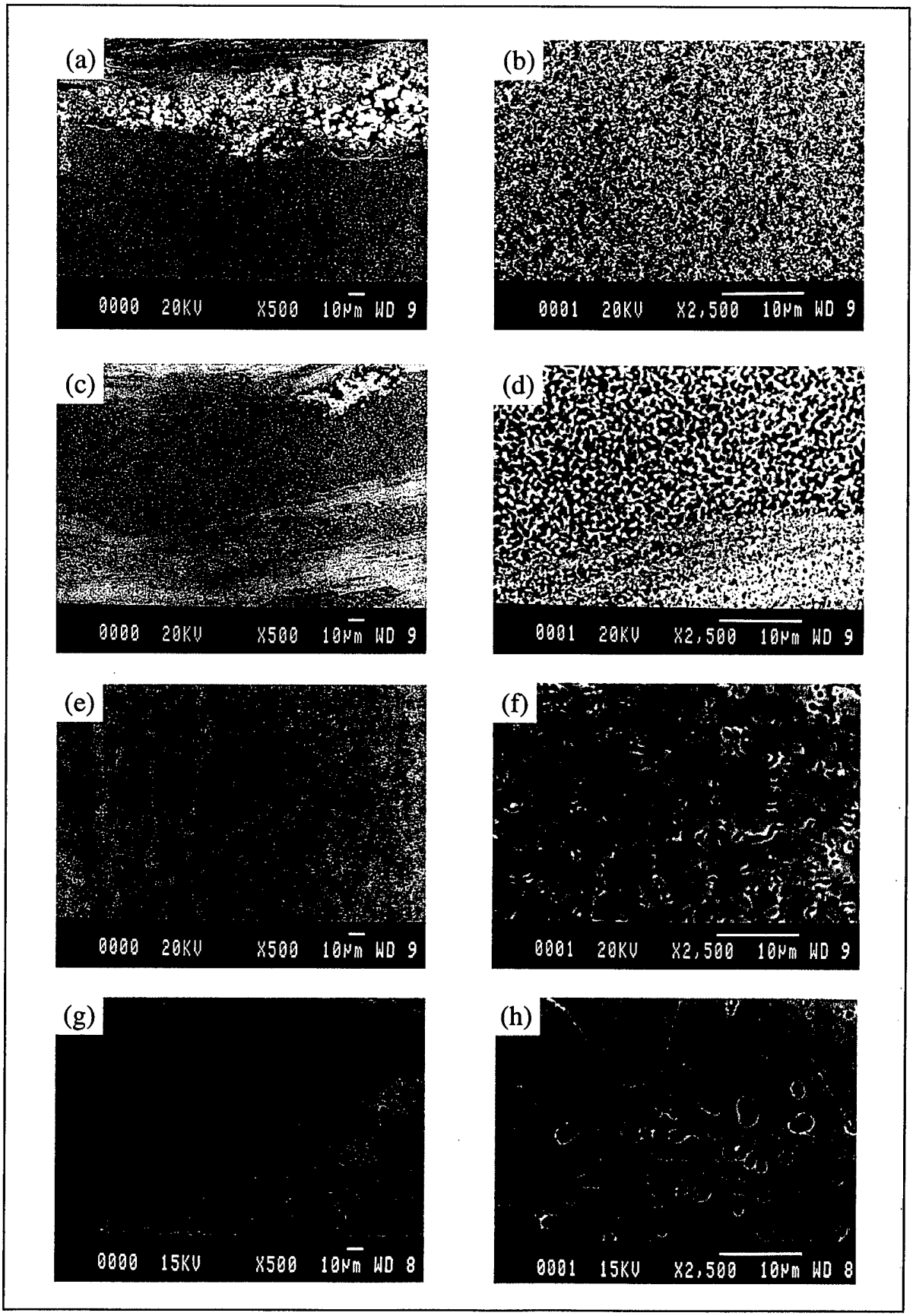

Figure 9. Backscattered electron micrographs of the pressureless sintered samples: (a) and (b) 300 °C, (c) and (d) 500 °C, (e) and (f) 700 °C, and (g) and (h) 900 °C.

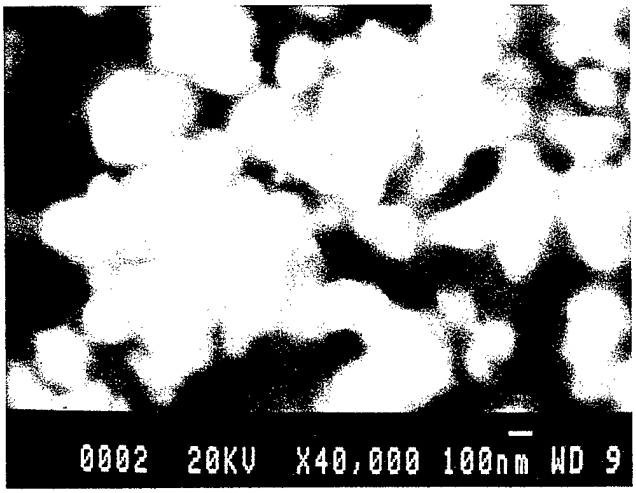

Figure 10. Higher magnification SEM view of the coarsened particles and particle-particle neck formation at 300 °C, below the secondary recrystallization temperature.

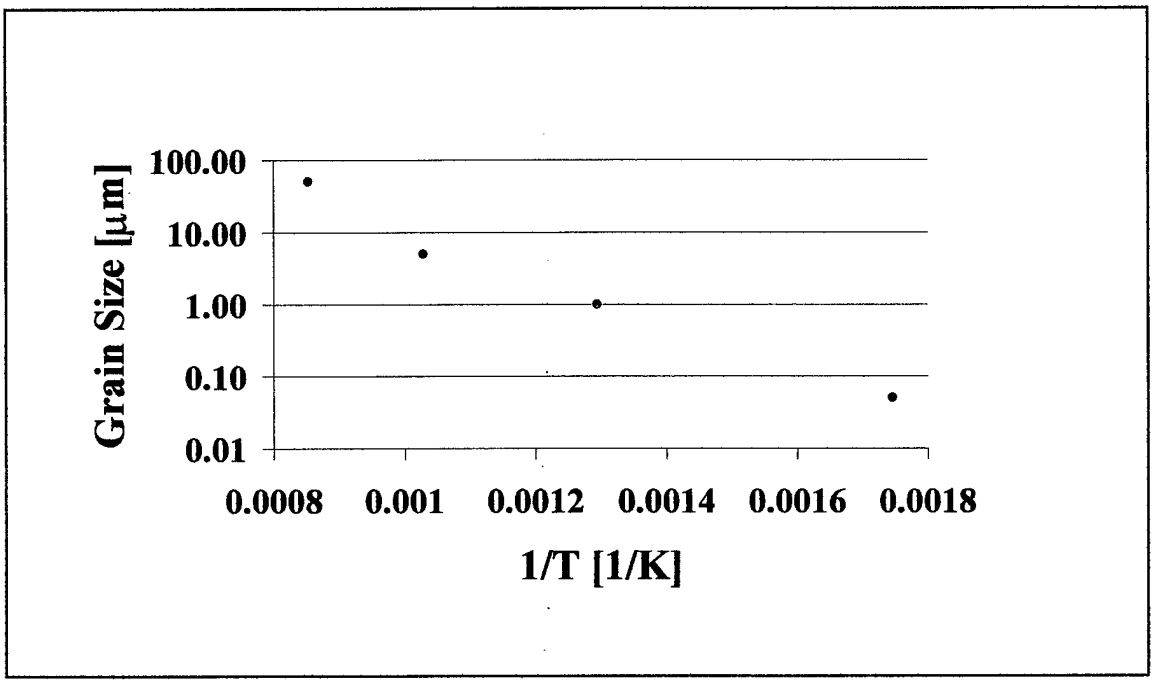

Figure 11. Grain size vs. inverse absolute temperature for the pressureless sintered samples.

Table 5. P^2C results.

Temperature (°C)	Time (min)	Pycnometry Density (gcm^{-3})	Density (% TD)
600	1	6.20	78.8
600	15	6.25	79.4
800	5	5.90	75.0
1000	1	6.06	77.0

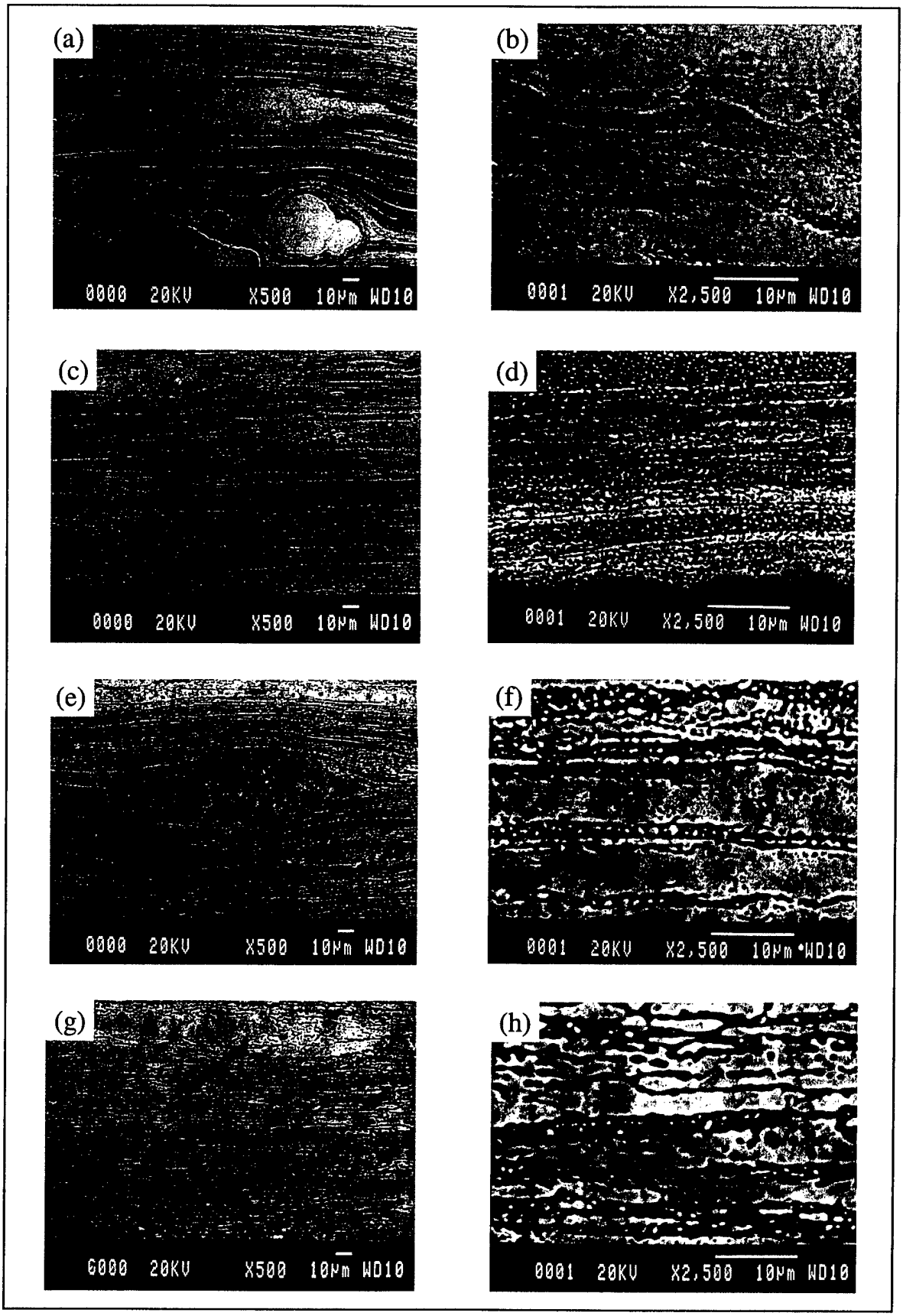

Figure 12. Low- and high-magnification SEM images of the P^2C samples are shown with 600 °C, 1 min in (a) and (b); 600 °C, 15 min in (c) and (d); 800 °C, 5 min in (e) and (f); and 1000 °C, 1 min in (g) and (h).

consists of 2- to 3-μm grains, interspersed with isolated submicrometer-sized porosity. Particles in less dense regions coarsen as well, resulting in a random distribution of isolated fine, nanosized droplets.

4. Discussion

4.1 Nanopowder Characterization

During the collection and evaluation of the particle size data it was quickly recognized that not all of the instruments provide first-hand or raw data output. Though statistically unsatisfactory, the electron optics-based observations instantaneously revealed the particle morphology and size information. In contrast, the BET and laser scattering techniques operate with factory-installed algorithms and geometrical models that require post-measurement interpretation related to the validity of the model. Lastly, the crystallographic methods required much more extensive user-based data fitting and analysis. Consequently, they do not readily lend themselves to the rapid assimilation and interpretation of the raw data.

Table 1 reported the summary of the mean particle sizes determined from all of the characterization methods. From the summary, it appears that the apparent, morphologically distinct Fe particle size is on the order of nanometers, ranging from roughly 25 to 80 nm. This is generally consistent with previous analyses of the powders [3]. However, the particles have a distinct fine structure and appear to cluster into much larger, micrometer-sized dendritic agglomerates. The evidence from FESEM of particle-particle necks along the dendritic arms, indicative of near-late-stage sintering, was left unexplained in the previous article [3].

This is quite understandable, notwithstanding the size of the particles, the enhanced sinteribility of nanopowders, and the excess heat available during the microwave sintering process. However, the available heat is limited because the internal crystal size within the particles appears to be smaller than their external dimensions. In other words, there is little or no indication of annealing within the grains.

As expected, FESEM yielded an adequate first-hand physical description of "typical" particle aggregates, though only semi-quantitative. The information gained with FESEM was more useful than that obtained with TEM because of the loss of surface detail in the latter. It may be noted that TEM also revealed a fine structure within the particles. Only, BET, the surface adsorption-based technique, identified the actual or functional particle size with a reasonable statistical variation. However, because BET is insensitive to macroscopic morphological arrangement of the particles, it failed to indicate the nature of agglomeration.

Neither SLS nor DLS could correctly identify the size or nature of the agglomeration. In part, this was attributed to the intrinsic properties of the Fe nanopowder agglomerates, the limitations in preparing the powder suspension, and the inherent inability to interpret scattering data from an open agglomerate structure by the analysis software. Further discrepancies between the SLS and DLS results may also be likely accountable by the differences in sampling methods. In SLS, the sample dispersion is circulated during the measurement; whereas, in DLS, it is not. That is, while in the SLS the agglomerates remain suspended, in the stationary cell of the DLS, the heavier particles will settle out. As a result, DLS would not detect any of the larger agglomerates. Further experiments such as sedigraphy may be needed to alleviate the disparity.

Both XRD and SANS/ND measurements, supported by TEM observations, resulted in a smaller particle size. This is most likely a measure of the crystal size within the particles. However, the ND/SANS with its greater penetration depth and resolution was able to identify at least two modes of crystallites within the sample.

4.2 Sintering and Densification

This study has shown that MPS does result in a powder with features on a nanometer scale. Aside from the large aggregates observed in FESEM, the BET surface area, and XRD measurements are consistent with a nanosized powder, as is the pyrophoricity of the powder during handling. However, despite little or no interior grain substructure as revealed in Figure 1 and supported by XRD analysis, the individual particles are sintered into stiff dendritic agglomerates.

The most striking properties of this MPS powder vis-á-vis a conventional powder are the unexpectedly low bulk green density, poor compaction, and sintering behavior. The high specific surface area of the primary particles cannot explain either the markedly low bulk density or the excessive springback. Both, however, can be understood as being due to the presence of the dendritic structures. The inability to compact the particles beyond a green density of 40% TD can also be attributed to these aggregates.

At temperatures below 500 °C, pressureless sintering cannot effectively remove the residual porosity from the as-pressed green compacts. Above 500 °C, nanoparticle grain growth is unavoidable, which is quickly superceded by secondary recrystallization, and, as a result, the initial precursor morphology is completely lost. This temperature is consistent with the conventional, secondary recrystallization temperature of 450 °C, T_R, for pure Fe [18].

It has been postulated that, due to increased interfacial and surface free energies in nanosized particles, sintering would be more enhanced at lower temperatures [3, 19]. The well-bonded particles within the dendritic arms seem to support this argument. The small value of Q_S seems to support this argument; however, the observed coarsening is more consistent with the behavior of larger, conventionally sized powders [20]. That is, no enhanced solid-state sintering, rearrangement, or concomitant densification took place at low temperatures. Instead, gain in

densification is seen only above T_R. This fact and the samples' structural heterogeneity (i.e., banding) are also a likely result of the initially dendritic agglomerates. It is believed that below T_R, as dictated by the lower Q_S, adjacent particles begin to rapidly neck, sinter, coalesce to form aggregate clusters. However, the spatial extent, bimodal particle size, and relative stiffness of the dendritic arms cause these clusters to become too widely spaced, thereby prevent any further possible collapse of the partly coarsened structure. Only at higher temperatures, with higher driving forces in place, the agglomerates collapse and an increase in density is realized. Thus, even if sufficient pressure would be brought to bear on the green body as to break up the agglomerates, it expected that a greater porosity would remain than in compacts made from conventional powders. Such porosity in the green compact is the most likely source of the large isolated pore clusters seen in Figures 8g and 8h. The use of the P^2C provides a little gain in densification, but with an added extrinsic, current-induced structural asymmetry that is imparted to the sintered body.

These results are inconsistent with those of Kalyanaraman et al. [3], where the starting material was prepared in an identical process, but consolidation was by the P^2C technique. In that study, heating a similar Fe starting material to temperatures around 900 °C at 65 MPa resulted in near full densification with grain sizes of >10 μm and a well-dispersed, uniform, 2- to 3-μm-sized residual porosity. However, the micrographs and density, reported in that reference, do not exhibit the heterogeneity seen here. The reason for this discrepancy is not immediately evident, but might be elucidated by further study.

Nevertheless, as has been said many times of powder characterization and consolidation, "What is generally required is not the size of the particles, but the value of some property of the particles that is size dependent. The final criteria are that the method shall measure the appropriate property of the particles [9]." For this Fe nanopowder, the extent and stiffness of the dendritic agglomeration was this property. Indeed, the thick interparticle necks within the agglomerates seen in Figure 1b are testimony to the enhanced sinterability of nanopowders. Unfortunately, the sinterability occurs at an inconvenient time during powder synthesis, whereby further processibility is compromised. It is suspected that modifications of MPS are required to sidestep this difficulty.

5. Summary and Conclusions

The size distribution of MPS Fe nanopowder was evaluated by several analytical methods. The nanopowder was found to consist of dendritic agglomerates that were difficult to disperse. Individual grains within the dendrite structures were dense and spherical. Further scrutiny and analysis indicated the existence of a finer subgrain structure with a bimodal size distribution within the particles. The estimated average particle size was 60–80 nm with 20-nm subgrains, while the overall agglomerate size was ~ 0.3–1 μm.

Consistent with many examples in larger-size powders, particle size determination in nanopowders was found to depend on the method used. Only FESEM and SLS provided information on the extent and morphology of agglomerates. Data from other methods were either complementary (BET and DLS) or provided detail (XRD and ND/SANS) beyond the required size and distribution information. Nevertheless, it is suggested that care be taken in making any of the measurements because, when viewed independently, the results may be misleading or erroneous.

The bimodal dendritic structure of the Fe nanopowder hindered the ability to consolidate into full-density structures. The initial size and morphology of the Fe was lost at a threshold temperature of 500 °C. An examination of the pressureless sintering behavior of this powder indicated that the dendritic structure of the nanopowder hinders solid-state sintering into a fully dense body. No enhanced sintering below the recrystallization temperature was observed. Using P^2C (high-DC current and low-pressure), the structure is stratified with a suppression of grain growth, however, without an increase in density. The implications are twofold: on one hand, if the nanostructure is to be retained, sintering must be conducted below this temperature. On the other hand, direct sintering of nanopowders to dense bodies will require more careful control of the MPS process to avoid formation of low-density agglomerates. While it may be possible to introduce further processing steps, for now, conventional pressing and pressureless sintering of such agglomerates to full-density bodies is extremely difficult.

6. References

1. Peigney, A., C. Laurent, O. Dumortier, and A. Rousset. "Carbon Nanotubes-Fe-Alumina Nanocomposites: Part I: Influence of the Fe Content on the Synthesis of Powders." *Journal of the European Ceramic Society*, vol. 18, pp. 1995–2004, 1998.

2. Phule, P. P. "Synthesis of Novel Magnetorheological Fluids." *Materials Research Society Bulletin,* vol. 23, no. 8, pp. 23–25, 1998.

3. Kalyanaraman, R., S. Yoo, M. S. Krupashnkara, T. S. Sudarshan, and R. J. Dowding. "Synthesis and Consolidation of Iron Nanopowders." *Nanostructured Materials,* vol. 10, no. 8, pp. 1379–1392, 1998.

4. Jia, D., K. T. Ramesh, and E. Ma. "Failure Mode and Dynamic Behavior of Nanophase Iron Under Compression." *Scripta Materialia,* vol. 42, no. 1, pp. 73–78, 2000.

5. Koch, C. C. "Synthesis of Nanostructured Materials by Mechanical Milling: Problems and Opportunities." *Nanostructured Materials,* vol. 9, no. 1, pp. 13–22, 1997.

6. He, L., L. F. Allard, K. Breder, and E. Ma. "Nanophase Fe Alloys Consolidated to Full Density From Mechanically Milled Powders." *Journal of Materials Research,* vol. 15, no. 4, pp. 904–912, 2000.

7. Groza, J. R. "Field-Activated Sintering." *ASM Handbook; Powder Metallurgy*, ASM, Materials Park, OH, vol. 7, pp. 583–589, 1998.

8. Jones, G., J. R. Groza, K. Yamazaki, and K. Shoda. "Plasma Activated Sintering (PAS) of Tungsten Powders." *Materials and Manufacturing Processes*, vol. 9, no. 6, pp. 1105–1114, 1994.

9. Allen, T. *Particle Size Measurement.* New York: Chapman and Hall, 1997.

10. Webb, P. A., and C. Orr. *Analytical Methods in Fine Particle Technology.* Norcross, GA: Micromeritics Instrument Corporation, 1997.

11. Geiger, G. "Selecting the Right Particle Size Analyzer." *American Ceramic Society Bulletin,* vol. 75, no. 7, pp. 44–48, 1996.

12. Singhal, A., G. Skandan, and R. J. Dowding. "A New Bench-Top Characterization Tool for Nanoparticulate Systems." *Scripta Materialia*, vol. 44, pp. 2203–2207, 2001.

13. Jiqiao, L., and H. Baiyun. "Particle Size Characterization of Ultrafine Tungsten Powder." *International Journal of Refractory Metals & Hard Materials*, vol. 19, pp. 89–99, 2001.

14. Klug, H. P., and L. E. Alexander. *X-ray Diffraction Procedures.* New York, NY: John Wiley & Sons, pp. 655–656 and 660–661, 1978.

15. Cullity, B. D. *Elements of X-ray Diffraction.* Reading, MA: Addison Wesley, pp. 284, 1978.

16. Klotz, B. R. "Characterization of Boron Carbide Consolidated by the Plasma Pressure Compaction (P^2C) Method." Master's thesis, Worcester Polytechnic Institute, Worcester, MA, 2001.

17. Gregg, S. J., and K. S. W. Sing. *Adsorption, Surface Area, and Porosity*, 2nd Edition. New York, NY: Academic Press, 1982.

18. Askeland, D. R. *The Science and Engineering of Materials.* Boston, MA: PWS-Kent Publishing Company, p. 123, 1989.

19. Groza, J. R., and R. J. Dowding. "Nanoparticulate Materials Densification." *Nanostructured Materials,* vol. 7, no. 7, pp. 749–768, 1996.

20. Goetzel, C. G. *Treatise on Powder Metallurgy: Vol. 1.* New York, NY: Interscience Publishers, Inc., p. 515, 1949.

Appendix. Detailed Notes on the Collection, Reduction, and Analysis of the Neutron-Based Diffraction and Scattering Data

A.1 Neutron Diffraction

The neutron diffraction measurements were performed with the BT1 multi-detector instrument located on the National Institute of Standards and Technology (NIST) Center for Neutron Research (CNR) reactor. The neutrons from the reactor are scattered by a single-crystal monochromator at a fixed scattering angle. This, now monochromatic, beam illuminates the sample. The neutrons scattered by the sample are detected by an array of 32 well-shielded detectors separated from each other by ~5° in scattering angle. This feature allows efficient collection of data. The instrument provides a choice of three monochromators. This results in different resolutions as function of scattering angle. The two monochromators used in the measurement were Cu (311) producing a wavelength of 1.5405 Å and Si (531) producing a wavelength of 1.5904 Å. The collimators before and after the monochromator and before the detectors were 7, 20, and 7 min of arc, respectively. The instrumental resolution was well measured as a function of scattering angle. The data were collected in 0.05° increments of scattering angle 2Θ. The Bragg law, relating the scattering angle at which a reflection occurs $2\Theta_{hkl}$, the characteristic length of that reflection d_{hkl}, and the wavelength λ is given by

$$\lambda = 2\, d_{hkl} \sin\Theta_{hkl}, \tag{A-1}$$

where (hkl) are the Miller indices of the reflection. It is more convenient to describe the independent variable as Q, the scattering vector, instead of 2Θ. Q is defined as

$$Q = 4\pi\sin\Theta/\lambda\,. \tag{A-2}$$

The Bragg law then is

$$Q = 2\pi/d. \tag{A-3}$$

The measured peak shape is described by a Gaussian function

$$I_{ND}(Q) = [I_{ND0}/(\sigma\sqrt{2\pi})]\exp\left(-(Q-Q_0)^2/2\sigma^2\right), \tag{A-4}$$

where Q_o is the peak position, and σ^2 is the variance. This variance in a diffraction pattern is determined by several factors. The most important of these are the instrumental resolution, and the size and strain of the particles. These two latter determine the intrinsic peak variance σ_I^2. The resolution determines σ_R^2. The measured variance σ^2 is related to these two by quadrature

$$\sigma^2 = \sigma_R^2 + \sigma_I^2. \tag{A-5}$$

The Q dependence of an intrinsic variance due to crystalline size has been developed by Scherrer[1] and that for lattice distortions by Wilson.[2] These treatments are well summarized by Klug and Alexander.[3] For particles of size S, the line is broadened such that

$$\sigma_S^2(Q) = \pi^2 K^2 / 2\ln(2) S^2, \tag{A-6}$$

where K is a shape parameter (whose value is close to 1 [which is the value used in the calculations]). In the case of lattice distortions, given a local strain, e, the peak will be shifted, in Q, from its unstrained value of Q_o by an amount δQ such that

$$e = Q/Q_o. \tag{A-7}$$

The variance of the lattice strain distribution e^2 will cause a broadening of the peak corresponding to

$$\sigma_e^2(Q) = e^2/Q_o^2. \tag{A-8}$$

Thus, the intrinsic variance is the sum of these two variances. In the present measurements, the values of S, e, and e^2 are obtained from the data.

A.2 Small Angle Neutron Scattering (SANS)

In all scattering measurements in which coherent interference effects are measured, the length scale, d, of inhomogeneities that produce the interference effects is given by

$$Q = 2\pi/d. \tag{A-3}$$

In order to attain sensitivity to a preferred size scale (i.e., 1 nm–300 μm), either large wavelengths or small angle measurement capability or both are needed. The 30-m SANS instruments available at CNR meets this requirement. A mechanical velocity selector renders the "cold neutrons" from the reactor source monochromatic. The monochromator provides a wavelength resolution of 10%–20%, and wavelengths from 5 to 12 Å. The small angle measurement capability is provided by the ability to define the direction of the incident and scattered neutrons. The incident direction is defined by two circular pinholes, which can be separated from each other by 3–15 m. The scattered neutron direction is defined by a two-dimensional detector whose sensitive area is arranged perpendicular to the incident direction. The spatial resolution of the detector is 5 mm. The angular and therefore Q range available in a measurement is determined by the position of the detector with respect to the sample. The detector can be placed at distances from 1–15 m from the sample and can be displaced 25 cm

---

[1] Scherrer, P. *Gott. Nachr.*, Vol. 2, p. 98, 1918.

[2] Wilson, A. J. C. "On Variance as a Measure of Line Broadening in Diffractometry .2. Mistakes and Stain." *Proceedings of the Physical Society of London*, vol. 81, no. 519, p. 41, 1963.

[3] Klug, H. P., and L. E. Alexander. *X-ray Diffraction Procedures*, New York, NY: John Wiley & Sons, pp. 655, 656, 660, 661, 1978.

laterally. The distance between the incident pinholes is adjusted to match the resolution determined by the sample-detector configuration.

The measured scattering pattern is a result of interference effects from the inhomogeneities in neutron scattering power present in the sample. In the present case, because the sample consists of Fe particles, these inhomogeneities result from the different scattering of neutrons by the Fe and the vacuum. It is for this reason that the size of the Fe particles is accessible by this technique. Formulating a model of the structures, of which the sample consists of, or is suspected to consist of, usually carries out the analysis of the scattering data. A calculation of the scattering resulting from this model is compared to the measured scattering, and the relevant parameters are adjusted until satisfactory agreement is achieved. Unless the particles are very uniform in both size and shape, the data are not capable of establishing unique information concerning the size and shape. The information is hidden in the integration. In this case, it is as useful to choose one shape as another. So, we choose the simplest (from the viewpoint of the calculation). The simplest is that of spheres of uniform density. In that case, the scattering cross-section per unit volume is given as

$$I_{SANS}(Q) = 9(\Delta\rho)^2\Phi V[\sin(Qr) - Qr\cos(Qr)]^2[Qr]^{-3}, \qquad \text{(A-9)}$$

where r is the sphere radius, V is the volume of the sphere, Φ is the volume fraction of the spheres in the sample, and $\Delta\rho$ is the scattering length density of the spheres. Actually, $\Delta\rho$ is the difference in the scattering length of the two media. However, because one of the media is the vacuum for which $\rho = 0$, $\Delta\rho$ is that for Fe ($\Delta\rho = 8.02 \times 10^{-6}$ Å^{-2}). If the sample consists of a distribution of spheres of different radii, then equation (A-9) is to be folded with the function describing this distribution.

A.3 Data Reduction and Analysis

As explained (equation [A-9]), a successful, rather an easy and straightforward, measure of the particle size with SANS will result if (1) the measured intensity saturates as Q tends to zero and (2) that several interference fringes are observed. The first indicates that the maximum particle size has been detected and the second that a narrow particle size distribution exists. A measurement of the scattering from the sample, with the 30-m SANS spectrometer at the NIST reactor, yielded ambiguous results. It was clear that the sample did not consist of spheres with a narrow distribution of radii. It was not clear what the true distribution was. Subsequently a high-resolution neutron diffraction measurement revealed the source of the difficulty and a characterization of the powder.

The measured diffraction pattern obtained from the Fe sample with the Cu (311) monochromator is presented in Figure A-1. All of the diffraction peaks correspond to the body-centered cubic Fe structure. The pattern obtained with the Si monochromator is not shown but has been used to confirm the results presented below. Each of the measured peaks consists of two components: a narrow large peak and a substantially broadened peak centered at approximately the same

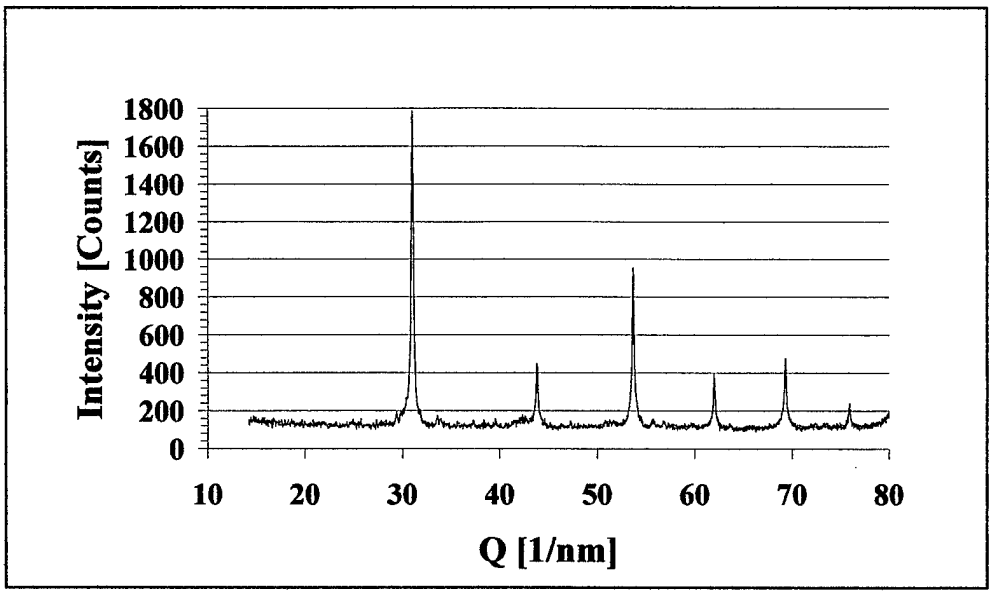

Figure A-1. The ND of the (Materials Modification Inc.) nanosized Fe powder.

position. Figure A-2 presents the (110) reflection. In that figure is also plotted the two components of which the feature consists. Both peaks are broader than the resolution. It is clear from Figure A-1 that the sample consists of at least two substantially different size particles.

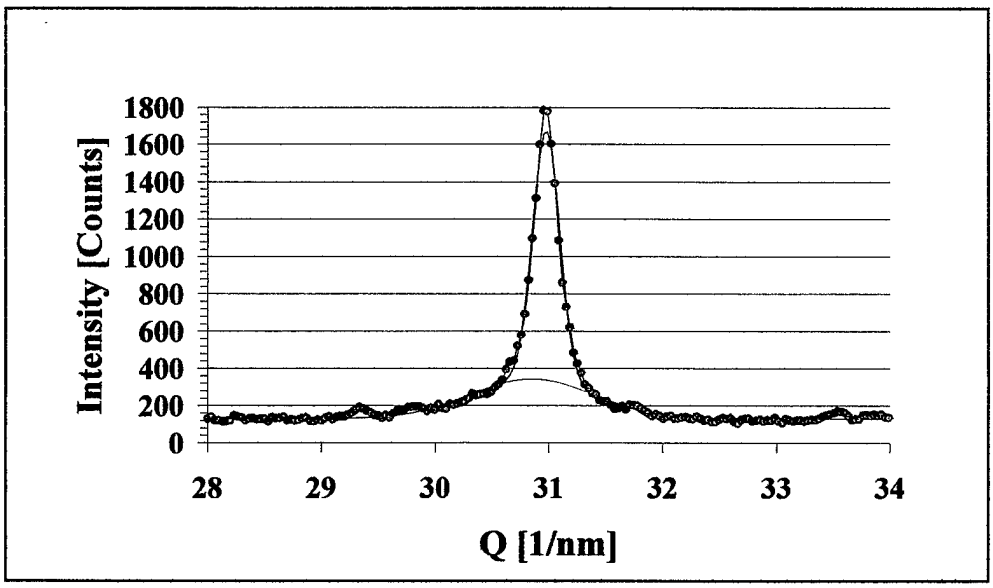

Figure A-2. The (110) peak in the diffraction pattern of the Fe nanopowder. The red and green solid lines are the two Gaussians used to fit the data.

This is the reason the SANS measurements were ambiguous. All the peaks obtained with both monchromators were treated in this manner, i.e., they were fit with two Gaussian functions. This analysis results in values of the integrated intensity, measured width and position of each of the two components as a function of Q. The integrated intensity reflects quantitatively the amount of

each component; the width is treated as indicated in order to obtain the size and strain variance conditions of that component and the position to obtain the residual strain. These results are presented in Figures A-3 and A-4. Figure A-3 presents the intrinsic standard deviation σ_I of the two components as a function of their position in Q. The solid lines are the result of the fit to the data with equations (A-6) and (A-8) as previously discussed. The parameters that produced the fits are presented in Table A-1. Here and in other values given, the numbers in parentheses correspond to one standard deviation in the least significant figure. With the exception of the value for the smallest Q, the data of Figure A-4 yields consistent values for the volume fraction of the large particles (narrow Q component) in the sample. Within one standard deviation, there is no residual strain in either component. The large particles constitute 37(5)% of the sample.

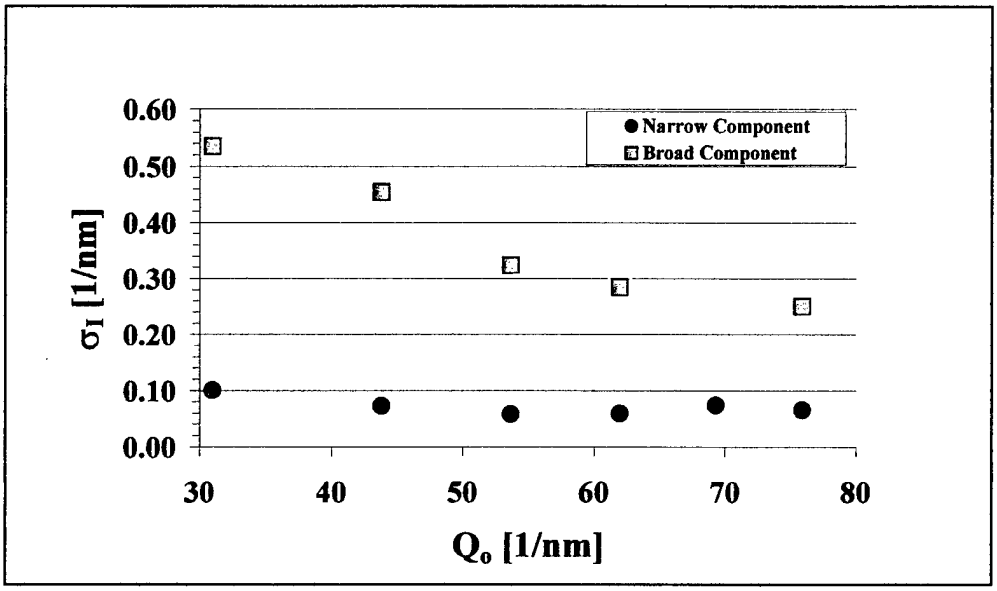

Figure A-3. The net Gaussian variance of the two Bragg peaks plotted as functions of Q. The lines are the result of fits to the data using equations (A-6) and (A-8). The parameters resulting from the fit are given in the text.

With this knowledge, we now return to the analysis of the SANS data. Because of the length scale to which the SANS data are sensitive (hundreds of Angstroms), only particle size and not information on strains can be obtained. We formulate a model that consists of a bimodal distribution of particle sizes as guided by the diffraction results. Each component is represented by a Schulz distribution4 whose parameters are scale factor, ISANS, mean particle size, r, and polydispersitivity, P. The model was then used to fit the SANS data. In the fitting process, only the scale factor and polydispersitivity were allowed to vary. The two r values used were those produced by the diffraction results. The result of the fit is shown in Figure A-5. In this figure, the data is shown as open circles, the model fit as a black line, and the contribution from each of

[4] Schulz, G. V. *Zeitschrift für physikalische Chemie.* Vol. 43, p. 25, 1935.

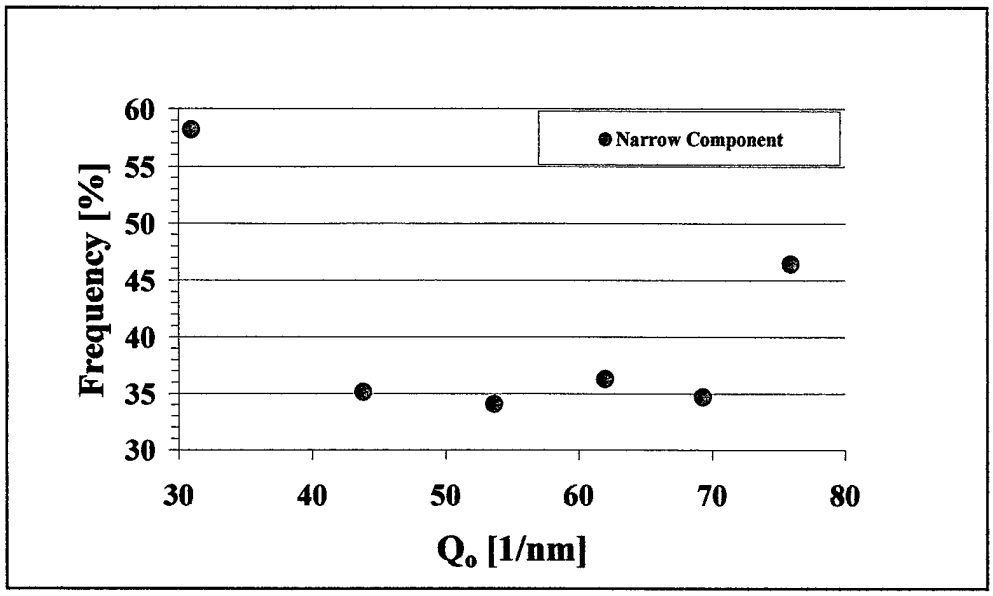

Figure A-4. The percent of the total intensity from the narrow component contribution.

Table A-1. Particle size of the nanosized Fe powder.

Component	Particle Size (Å)
Narrow	630(17)
Broad	243(31)

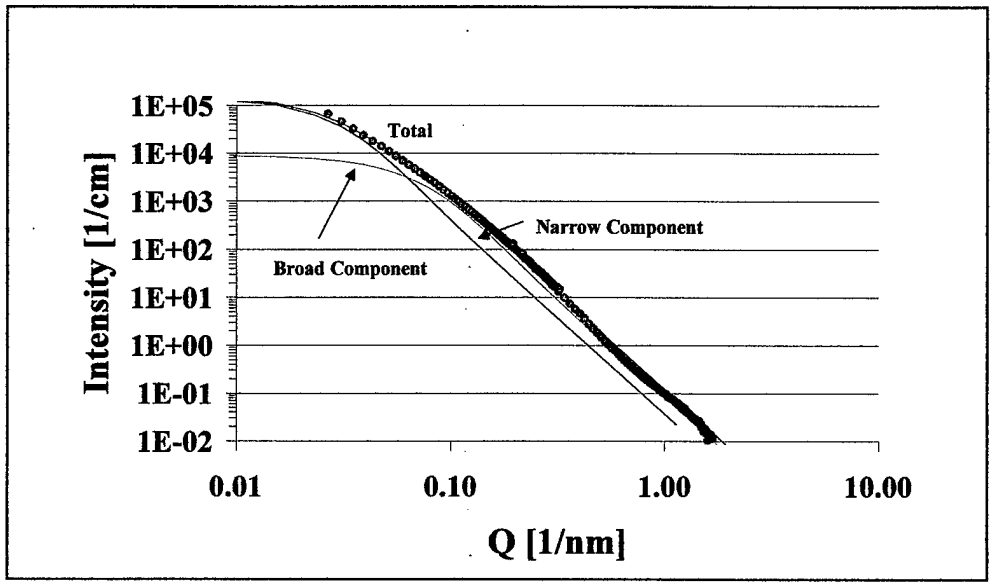

Figure A-5. The SANS data and the respective fits resulting from the bimodal distribution.

the distributions by blue (small particles) and red (large particles). The shape of the data may be seen as innocuous; this is of course the fault of the sample whose properties we intend to discover. There are two features that contain the essential information. These are a broad concave curvature at Q ~0.01 Å and a convex curvature at Q ~0.06 Å. The requirement that these be reproduced results in the determination of the polydispersitivity. In any case, the resulting particle size distribution is shown in Figure A-6 in which the distribution for each component is also shown. The scale factors indicate that the large component is ~47% of the total rather than the ratio resulting from the diffraction data. We do not consider this to be debilitating in so far as being able to assert that the two data sets are consistent and that the model is faithful.

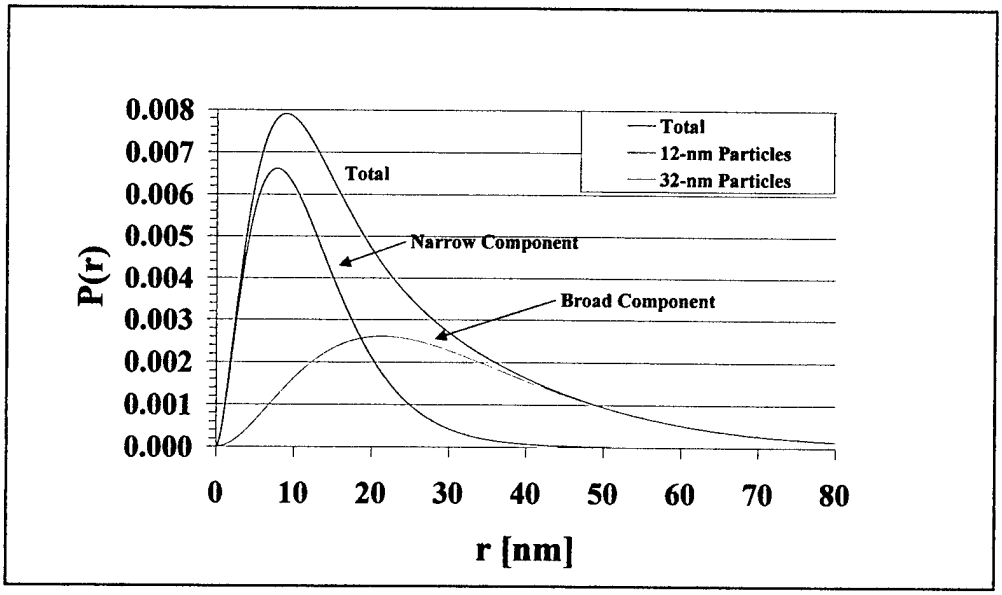

Figure A-6. The total particle size distribution resulting from a fit to the SANS data. The individual distributions of the two components are also shown.

Report Documentation Page

Form Approved
OMB No. 0704-0188

1. REPORT DATE *(DD-MM-YYYY)*	2. REPORT TYPE	3. DATES COVERED (From - To)
February 2003	Final	May 1999–October 2002

4. TITLE AND SUBTITLE
The Sintering and Densification Behavior of an Iron Nanopowder Characterized by Comparative Methods

5a. CONTRACT NUMBER

5b. GRANT NUMBER

5c. PROGRAM ELEMENT NUMBER

6. AUTHOR(S)
Laszlo J. Kecskes, Robert H. Woodman, Samuel F. Trevino, Bradley R. Klotz, and S. Gary Hirsch

5d. PROJECT NUMBER
1L622105AH84-622195A

5e. TASK NUMBER

5f. WORK UNIT NUMBER

7. PERFORMING ORGANIZATION NAME(S) AND ADDRESS(ES)
U.S. Army Research Laboratory
Weapons and Materials Research Directorate
Aberdeen Proving Ground, MD 21005-5069

8. PERFORMING ORGANIZATION REPORT NUMBER
ARL-TR-2909

9. SPONSORING/MONITORING AGENCY NAME(S) AND ADDRESS(ES)

10. SPONSOR/MONITOR'S ACRONYM(S)

11. SPONSOR/MONITOR'S REPORT NUMBER(S)

12. DISTRIBUTION/AVAILABILITY STATEMENT
Approved for public release; distribution is unlimited.

13. SUPPLEMENTARY NOTES

14. ABSTRACT

Fe nanopowder, derived from microwave plasma synthesis (Materials Modifications Inc., Fairfax, VA), was obtained and characterized for particle size and size distribution. The methods used included static light scattering (SLS) and dynamic light scattering (DLS), surface area and size by Brunauer, Emmett, and Teller (BET) analysis, small angle neutron scattering (SANS), neutron diffraction (ND), x-ray diffraction (XRD), field emission scanning electron microscopy (FESEM), and transmission electron microscopy (TEM). Based on these methods, it was concluded that the Fe powder was composed of nanosized particles, but in micrometer-sized aggregates. DLS indicated a mean agglomerate size with a single mode distribution of 70 ± 6 nm. In contrast, SLS revealed a wide bimodal distribution ranging from 0.5 to 20 μm. The mean particle sizes that resulted from BET and XRD analyses were 60 and 20 nm, respectively. SANS, in combination with ND, determined that the powder had a bimodal distribution of mean size 24 and 64 nm. TEM and FESEM confirmed that the powder is composed of 50- to 80-nm particles that is found in large, dendritic particle agglomerates which are on the order of micrometers.

Subsequent to characterization, the sinterability and densification behavior of the Fe nanopowder was examined by further experimentation wherein powder compacts were pressureless sintered under hydrogen. Results showed that without pressure, the powder could not be sintered to full density, however, the densification of the Fe powder strongly depended on the temperature. There was little or no coarsening below 500 °C. In contrast, significant grain growth was observed in the samples above that temperature. In further experiments, using a plasma pressure compaction (P^2C) apparatus, the powder was consolidated to final densities near 80% of the theoretical full density. The observed limitations in the densification and associated porous microstructures of the pressureless-sintered and P^2C-densified compacts were rationalized in terms of the

15. SUBJECT TERMS
nanopowder, characterization, microscopy, surface area measurement, laser scattering, Fe, density, microstructure, consolidation, sintering, plasma-activated sintering, pressureless sintering, grain growth

16. SECURITY CLASSIFICATION OF:			17. LIMITATION OF ABSTRACT	18. NUMBER OF PAGES	19a. NAME OF RESPONSIBLE PERSON
a. REPORT	b. ABSTRACT	c. THIS PAGE			Laszlo J. Kecskes
UNCLASSIFIED	UNCLASSIFIED	UNCLASSIFIED	UL	40	19b. TELEPHONE NUMBER *(Include area code)* (410) 306-0811

INTENTIONALLY LEFT BLANK.